

Water Resources Research



RESEARCH ARTICLE

10.1029/2021WR030943

Flushing the Lake Littoral Region: The Interaction of Differential Cooling and Mild Winds

Cintia L. Ramón^{1,2} , Hugo N. Ulloa^{3,4} , Tomy Doda^{2,4} , and Damien Bouffard¹ 

¹Department of Surface Waters – Research and Management, Eawag (Swiss Federal Institute of Aquatic Science and Technology), Kastanienbaum, Switzerland, ²Water Research Institute and Department of Civil Engineering, University of Granada, Granada, Spain, ³Physics of Aquatic Systems Laboratory, EPFL (École Polytechnique Fédérale de Lausanne), Lausanne, Switzerland, ⁴Department of Earth and Environmental Science, University of Pennsylvania, Philadelphia, PA, USA

Key Points:

- Previous parameterizations for cross-shore discharges driven by differential-cooling in lake littoral regions assume calm wind conditions
- Even mild cross-shore winds ($\lesssim 5 \text{ m s}^{-1}$) modify the convective circulation in the lake littoral region
- Upwind and downwind net cross-shore discharges can be predicted by the sum of the cooling and wind-driven contributions

Supporting Information:

Supporting Information may be found in the online version of this article.

Correspondence to:

C. L. Ramón,
crcasanas@ugr.es

Citation:

Ramón, C. L., Ulloa, H. N., Doda, T., & Bouffard, D. (2022). Flushing the lake littoral region: The interaction of differential cooling and mild winds. *Water Resources Research*, 58, e2021WR030943. <https://doi.org/10.1029/2021WR030943>

Received 29 JUL 2021
Accepted 11 FEB 2022

Author Contributions:

Conceptualization: Cintia L. Ramón, Damien Bouffard
Investigation: Cintia L. Ramón, Hugo N. Ulloa
Methodology: Cintia L. Ramón, Hugo N. Ulloa
Project Administration: Damien Bouffard
Validation: Cintia L. Ramón
Writing – original draft: Cintia L. Ramón, Hugo N. Ulloa, Tomy Doda, Damien Bouffard

Abstract The interaction of a uniform cooling rate at the lake surface with sloping bathymetry efficiently drives cross-shore water exchanges between the shallow littoral and deep interior regions. The faster cooling rate of the shallows results in the formation of density-driven currents, known as thermal siphons, that flow downslope until they intrude horizontally at the base of the surface mixed layer. Existing parameterizations of the resulting buoyancy-driven cross-shore transport assume calm wind conditions, which are rarely observed in lakes and thereby restrict their applicability. Here, we examine how moderate winds ($\lesssim 5 \text{ m s}^{-1}$) affect this convective cross-shore transport. We derive simple analytical solutions that we further test against realistic three-dimensional numerical hydrodynamic simulations of an enclosed stratified basin subject to uniform and steady surface cooling rate and cross-shore winds. We show cross-shore winds modify the convective circulation, stopping or even reversing it in the upwind littoral region and enhancing the cross-shore exchange in the downwind region. The analytical parameterization satisfactorily predicted the magnitude of the simulated offshore unit-width discharges in the upwind and downwind littoral regions. Our scaling expands the previous formulation to a regime where both wind and buoyancy forces drive cross-shore discharges of similar magnitude. This range is defined by the non-dimensional Monin-Obukhov length scale, χ_{MO} : $0.1 \lesssim \chi_{MO} \lesssim 0.5$. The information needed to evaluate the scaling formula can be readily obtained from a traditional set of in situ observations.

Plain Language Summary The flushing of the littoral region is a fundamental question for local lake managers. From a physical viewpoint, exchanges between littoral and pelagic regions are largely dominated by horizontal currents. Existing parameterizations of the cross-shore transport commonly reduce the problem to a single forcing mechanism. Wind-driven circulation is generally the main factor explaining the flushing of shallow waters in lakes. Yet, another forcing such as differential cooling resulting from a uniform surface cooling exerted on waterbodies of varying bathymetry also drives cross-shore transport. Briefly, shallow littoral waters become denser and generate a cross-shore circulation cell, with denser littoral water flowing offshore near the lake bed and lighter interior water moving onshore near the surface. However, this “thermal siphon” often co-occurs with moderate winds ($\lesssim 5 \text{ m s}^{-1}$) that drive cross-shore water exchanges of similar magnitude, limiting the applicability of existing parameterizations. Here, we focus on the thermal-siphon-wind interaction regime. We derive simple analytical solutions that are satisfactorily tested against real-scale three-dimensional numerical hydrodynamic simulations of an enclosed stratified basin subject to uniform and steady surface cooling rate and cross-shore winds. Our scaling improves the estimations of the cross-shore exchange in the interaction regime.

1. Introduction

The lake littoral region is the transition zone between the lake watershed and lake pelagic waters and is thus particularly vulnerable to land use. The effect of land use on downstream waters is a well-known issue that goes back long in history. For instance, the large-scale Roman deforestation and farming in Lake Murten (Switzerland) catchment led to its first eutrophication (Haas et al., 2019). Two millennia after, eutrophication resulting from uncontrolled nutrient loading remains a severe issue at a global scale that has fundamentally modified the lake ecology (e.g., Carpenter et al., 1998). Land-use effects also concern heavy metals (Fitchko & Hutchinson, 1975; Thevenon et al., 2011) and more recently micropollutants (Bonvin et al., 2011; Kandie et al., 2020; Perazzolo et al., 2010) and microplastics (Li et al., 2018; Sighicelli et al., 2018). This list of ecologically misplanned

© 2022 The Authors.

This is an open access article under the terms of the [Creative Commons Attribution-NonCommercial License](https://creativecommons.org/licenses/by-nc/4.0/), which permits use, distribution and reproduction in any medium, provided the original work is properly cited and is not used for commercial purposes.

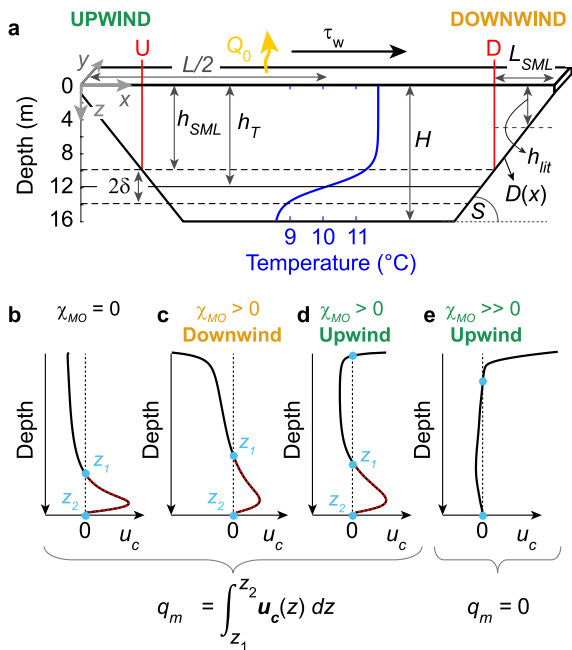


Figure 1. Model domain and calculations of offshore bottom flow. (a) Schematic of the model domain, initial temperature profile, and relevant length scales. Note that the vertical coordinate z has its origin ($z = 0$) at the lake surface and increases downwards, that is, $z = \text{depth}$. The lake has a constant width (y -direction) and depth is only varying in the x -direction. The average depth of the littoral region is defined as $h_{lit} = L_{SML}^{-1} \int_0^{L_{SML}} D(x) dx$. (b–e) Schematic of possible cross-shore velocity profiles in the littoral region highlighting in red the integration region for the calculations of the modeled offshore discharges q_m . Light blue dots in (b–e) mark the location of stagnation points in each profile.

et al., 1990) and has been viewed as an important mechanism connecting the littoral and interior regions during calm conditions in lakes (Fer et al., 2001; Woodward et al., 2017) and oceanic coastal waters (e.g., Shapiro et al., 2003). For example, Fer et al. (2001) estimated from an upscaling of their local observations that the volume flux transported by thermal siphons (hereon TSs) in Lake Geneva (Switzerland) in winter is $O(10)$ times the mean winter flow by rivers into the lake.

The flow, discharge per unit width, from the littoral region due to differential cooling depends on the magnitude of the surface buoyancy flux, B_0 , and the geometry of the littoral region, as shown for example, in the laboratory experiments by Sturman and Ivey (1998) and Sturman et al. (1999), and more recently in the theoretical and modeling study by Ulloa et al. (2022). Specifically, Sturman and Ivey (1998) adapted the seminal Phillips (1966) similarity solution for convective turbulent flows driven by uniform buoyancy flow in the presence of side boundaries and proposed that the steady-state discharge q_c could be estimated, as:

$$q_c = ah_{lit}(B_0 L_{SML})^{1/3}, \quad (1)$$

In which a is a proportionality coefficient varying from ≈ 0.1 to ≈ 0.4 (e.g., Doda et al., 2022; Harashima & Watanabe, 1986; Sturman & Ivey, 1998), h_{lit} is the average depth of the littoral region and L_{SML} is the length of the littoral region (Figure 1a). This scaling assumes zero wind stress; that is, calm conditions, rarely met in nature. Several field-based and modeling works have already reported that wind could block or enhance TSs (James et al., 1994; Mahjabin et al., 2019; Molina et al., 2014; Monismith et al., 1990; Roget et al., 1993; Rueda et al., 2007; Sturman et al., 1999; Woodward et al., 2017). For example, Sturman et al. (1999) reported that TSs in Australian shallow wetlands were “consistently observed” when wind speeds dropped below 3 m s^{-1} . Rueda et al. (2007) modeled differential cooling in a lagoon in Southern Spain and showed that winds weaker than 3 m s^{-1} could still slow down TSs. Woodward et al. (2017) modeled a cooling period in an Australian reservoir and

land use ultimately affecting downstream waters goes on, and, today, lakes are well recognized as integrators of the watershed. Besides the already mentioned allochthonous contamination, the littoral region acts as an internal reactor for autochthonous processes affecting nutrient, organic matter, and gas cycles (e.g., Hofmann, 2013; Hofmann et al., 2010; James & Barko, 1991; Yakimovich et al., 2020). The fate and final impact of allochthonous or autochthonous compounds on the water quality depends on their residence time in the littoral region. This residence time is controlled by horizontal currents connecting the littoral and the pelagic zones (e.g., Rao & Schwab, 2007).

Horizontal exchanges result from different forcings. Wind stress acting on the lake surface is often considered the main driver with direct (hereon wind circulation; e.g., Bengtsson, 1978) and indirect transport processes (e.g., basin-scale internal waves; Coman & Wells, 2012; Marti & Imberger, 2008). In the vicinity of river inflows, inertial and buoyancy forces from riverine waters are also an important localized source of horizontal exchanges (e.g., Cortés et al., 2014; Hogg et al., 2013). Finally, spatial differences in the meteorological forcing across the lake (e.g., Verburg et al., 2011) or cross-shore gradients in lake depths (Mao et al., 2019; Monismith et al., 1990) lead to differential cooling or heating that generates large horizontal exchanges. In the latter case, the shallower littoral region will heat or cool at a faster rate than the pelagic waters, yet, exposed to the same uniform air-water heat exchange rate. The resulting horizontal density gradient leads to horizontal water exchanges between the two regions. Here, we focus on periods of lake cooling, when the lake water is above the temperature of maximum density ($T \approx 4^\circ\text{C}$). The colder littoral region triggers density-driven currents that transport littoral water downslope and intrude horizontally at the base of the surface mixed layer (e.g., Doda et al., 2022; Fer et al., 2001) or even at deeper depths for weak thermoclines, potentially contributing to deep water renewal (Biemond et al., 2021; Lemmin, 2020; Peeters et al., 2003). This particular type of density-driven flow is called thermal siphons (Monismith

reported that “pure” TSs occur for winds lower than $\approx 2.4 \text{ m s}^{-1}$, while a combined flow, mix of wind-driven and convectively driven flow, occurred for wind speeds between 2.4 and 4.5 m s^{-1} . These examples suggest that there is a regime where both wind and buoyancy forces are equally important in driving the cross-shore circulation. In this regime, and depending on the wind direction, the strength of the TSs could be weakened or reinforced and Equation 1 would fail to predict the magnitude of the cross-shore discharge. Therefore, a practical expression that accounts for both cooling and wind-stress effects is lacking.

Our goal is to provide a practical equation to predict the cross-shore discharge, q , due to the interaction of uniform surface cooling and mild cross-shore directed winds acting in enclosed stratified basins. Here, we couple a scaling-based analysis with numerical experiments to determine and evaluate a practical mathematical expression of the form $q_{\text{total}} = q_c + q_w$, that accounts for the cooling- (q_c) and wind-driven (q_w) contributions for the net cross-shore discharge. Our results illustrate that this simple linear expression has successful predicting skills in shallow and elongated lakes under steady forcing conditions.

2. Materials and Methods

2.1. Wind-Convection Interaction Regime

In this study, our reference is the cross-shore flow resulting from differential cooling (Equation 1) and we examine how mild winds modify the established convective circulation in a stratified basin. For this, the Monin-Obukhov length scale, L_{MO} , is nondimensionalized and used to define the regime of interaction between convectively and wind-driven flows:

$$\chi_{\text{MO}} = \frac{L_{\text{MO}}}{h_{\text{SML}}} = \frac{u_*^3}{k B_0 h_{\text{SML}}} = \frac{u_*^3}{k w_*^3}, \quad (2)$$

where u_* is the surface friction velocity, defined as $u_* = (\tau_w / \rho_0)^{1/2}$ (e.g., Wüest & Lorke, 2003), τ_w is the surface wind shear stress, ρ_0 is a reference density, k (≈ 0.41) is the von Kármán constant, h_{SML} is the depth of the surface mixed-layer (hereon SML) and w_* is the convective velocity scale, defined as $w_* = (B_0 h_{\text{SML}})^{1/3}$ (Deardorff, 1970). L_{MO} represents the depth scale over which shear dominates over convection in driving the deepening of the SML and χ_{MO} its proportion with respect to the actual SML depth. Thus, as χ_{MO} reaches values above unity, wind shear overcomes convection and becomes the leading vertical mixing mechanism. Considering that the flow speed of TSs in sloping basins scales as $u_c \sim (B_0 L_{\text{SML}})^{1/3} \sim w_* (L_{\text{SML}}/h_{\text{SML}})^{1/3}$, Equation 2 also provides a quantification of the relative importance of wind in driving the exchange flows in littoral regions subject to surface cooling. For values of χ_{MO} tending toward zero, the effect of the wind is negligible and the exchange flow can be estimated by Equation 1. For $\chi_{\text{MO}} \text{ O}(1)$, wind-driven flows dominate the cross-shore circulation. In the case of temperate lakes, χ_{MO} varies from $\text{O}(10^{-2})$ to $\text{O}(10)$ (e.g., Read et al., 2012). Here, we explore the range of χ_{MO} values delimiting the interaction regime.

2.2. Hydrodynamic Model

Simulations were conducted with the three-dimensional (3-D) non-hydrostatic z-coordinate RANS model MITgcm (MIT General Circulation Model, Marshall, Adcroft, et al., 1997; Marshall, Hill, et al., 1997 and details in <http://mitgcm.org>). MITgcm solves the Navier-Stokes equations with a finite-volume discretization and under the Boussinesq approximation. An Arakawa-C grid is used to discretize the momentum equations and a quasi-second-order Adams-Bashforth time-stepping scheme is used to advance the variables in time. MITgcm has been shown to successfully reproduce density-driven currents due to differential cooling in coastal sea waters (Biton et al., 2008) and differential heating under lake ice (Ramón et al., 2021). Ramón et al. (2021) conducted a detailed model validation/calibration with large eddy simulation data. We adopted here the same model configuration as in Ramón et al. (2021) which is summarized in the following lines. We used the non-hydrostatic capabilities of the code to resolve convective cells, which contribute to enhancing turbulent mixing in the SML. Water density was determined from temperature using a nonlinear equation of state (McDougall et al., 2003). The advection terms in the transport equation for temperature were discretized with the nonlinear third order DST (direct space-time) with a flux limiter. The 3-D Smagorinsky approach with a constant of 0.0005 was used to parameterize horizontal and vertical viscosities. Background vertical viscosities were set to $10^{-6} \text{ m}^2 \text{ s}^{-1}$. Background values for the grid-dependent nondimensional lateral viscosities were set to 0.002. For a horizontal grid resolution of 2 m

and a time step of 0.5 s, this is equivalent to horizontal eddy viscosity of $\approx 4 \times 10^{-3} \text{ m}^2 \text{ s}^{-1}$. Background horizontal and vertical diffusivities for heat were set to $10^{-5} \text{ m}^2 \text{ s}^{-1}$ and $1.4 \times 10^{-7} \text{ m}^2 \text{ s}^{-1}$. No-slip conditions were applied at all lateral vertical walls and the bottom. A detailed description of the sensitivity of the modeled convective unit-width discharges q_c to the selected background horizontal viscosities is included in the Supporting Information S1, which could introduce variability in q_c of as much as 35%. This uncertainty has an effect on the actual value of constant a in Equation 1, but does not affect the main conclusions of this study. For reproducibility purposes, all MITgcm input files used in this study can be accessed (see link in Acknowledgments).

2.3. Lake Model

To evaluate the effect of wind stress in the development of TSs in a lake, we chose an elongated trapezoidal bathymetry (Figure 1a) of constant width, where depth varies only in the x -direction (see reference coordinate system in Figure 1a). This quasi 2-D configuration reduces the magnitude of currents in the y -direction (i.e., alongshore direction, Figure 1a) and has two symmetric littoral regions (downwind and upwind littoral regions, respectively) allowing to evaluate, in each simulation, the effect of both a favorable and opposing wind stress to the convectively driven circulation of the lake.

Nearshore slopes of $O(10^{-2})$ are commonly found in lakes and depths of $O(10)$ m are characteristic of shallow lakes. Our idealized basin holds these features and its geometry is, for example, similar to Lake Rotsee, a small temperate Swiss lake where TSs have been observed (Doda et al., 2022). The lake's total length and width are 1,800 and 180 m, respectively. The littoral region depth, $D(x)$, increases in the x -direction from 1 m to $H = 16$ m, the maximum depth of the lake, with a longitudinal slope $S = 0.03$ (Figure 1a). The lake domain, with a total of $\approx 9.8 \times 10^6$ wet cells, was discretized using a horizontally uniform Cartesian grid ($\Delta x = \Delta y = 2$ m) with vertically variable thickness (Δz). Δz increases with depth from $\Delta z = 0.05$ m within the first 2 m to cells of 0.2 m in the bottom 6 m.

The lake is initially at rest, with horizontal isotherms. The initial temperature profile follows a hyperbolic tangent function (Equation 3):

$$T(z) = T_b + \frac{(T_0 - T_b)}{2} \tanh\left(\frac{h_T - z}{\delta} + 1\right), \quad (3)$$

where T_0 ($= 11.7^\circ\text{C}$) and T_b ($= 8.5^\circ\text{C}$) are the surface and bottom temperatures in the initial profile, and h_T ($= 11.9$ m) and 2δ ($= 4$ m) are the fitted location of the center of the thermocline and the metalimnion width, respectively (Figure 1a). The initial depth of the surface mixed layer is then $h_{\text{SML},0} = h_T - \delta = 9.9$ m (Figure 1a). This initial temperature profile is, for example, representative of late-autumn conditions in Rotsee (Doda et al., 2022). The progressive deepening of the surface mixed layer was tracked by fitting Equation 3 to the temperature profile at the lake center at each time step after removing near-surface values where temperature increases with depth ($dT/dz > 0$). Temperature boundary conditions are prescribed as adiabatic, except at the surface, where heat exchange occurs between the waterbody and the atmosphere. The heat loss rate at the surface, Q_0 , was set to 200 W m^{-2} , a magnitude broadly observed in temperate lakes (e.g., Doda et al., 2022; Fer et al., 2002; MacIntyre & Melack, 2009). The surface buoyancy flux was then estimated as $B_0 = \alpha g Q_0 / (\rho_e C_p)$, where α is the thermal expansivity of the surface water, g is the gravitational acceleration, ρ_e is the epilimnetic water density and C_p is the specific heat of water. For the selected Q_0 , $B_0 = 5.2 \times 10^{-8} \text{ W kg}^{-1}$ and $w_* = 8 \times 10^{-3} \text{ m s}^{-1}$. B_0 $O(10^{-8} - 10^{-7}) \text{ W kg}^{-1}$ are typical of cooling periods in temperate lakes (e.g., Doda et al., 2022; Fer et al., 2002; Rueda et al., 2007).

Numerical experiments (Table 1) were initially run by only considering surface cooling until the thermally driven cross-shore flow was stabilized. This timescale was determined a priori using the adjustment timescale derived from the first principles by Ulloa et al. (2022). For a wedge-shaped littoral region, the quasi-steady state should be reached at:

$$t_{\text{SS}} = \frac{2L_{\text{SML}}}{(B_0 L_{\text{SML}})^{\frac{1}{3}}} \left(1 - \frac{h_{\text{min}}}{h_{\text{SML}}}\right)^{-\frac{1}{3}}. \quad (4)$$

Table 1
Run Cases

Run	χ_{MO}	u_* (m s ⁻¹)	τ_w (N m ⁻²)	u_{10} (m s ⁻¹) ^a
0	0	0	0	0
1	1×10^{-3}	6.0×10^{-4}	3.6×10^{-4}	0.04
2	2.8×10^{-2}	1.8×10^{-3}	3.2×10^{-3}	0.54
3	6.6×10^{-2}	2.4×10^{-3}	5.8×10^{-3}	1.09
4	1.3×10^{-1}	3.0×10^{-3}	9.0×10^{-3}	1.82
5	3.1×10^{-1}	4.0×10^{-3}	1.6×10^{-2}	3.58
6	5.3×10^{-1}	4.8×10^{-3}	2.3×10^{-2}	4.33
W1	-	6.0×10^{-4}	3.6×10^{-4}	0.04
W2	-	1.8×10^{-3}	3.2×10^{-3}	0.54
W3	-	2.4×10^{-3}	5.8×10^{-3}	1.09
W4	-	3.0×10^{-3}	9.0×10^{-3}	1.82
W5	-	4.0×10^{-3}	1.6×10^{-2}	3.58
W6	-	4.8×10^{-3}	2.3×10^{-2}	4.33

Note. Initial χ_{MO} values and wind forcing.

^a u_{10} is the wind velocity at 10 m height above the water surface calculated as $u_{10} = [\tau_w / (\rho_{air} C_d)]^{1/2}$, where ρ_{air} is the air density (= 1.23 kg m⁻³) and the wind drag coefficient, C_d , is a function of u_{10} (Wüest & Lorke, 2003).

Here h_{min} is the minimum depth of the littoral region (=1 m). All the above and the other key length scales used in this study are listed in Table 2. With an initial L_{SML} of ≈ 297 m, t_{SS} should be ≈ 7 hr. Once TSs were fully developed and reached a quasi-steady state, constant wind stress, τ_w , in the direction of the main lake axis (x -direction) was applied with a ramp-up period of 1 hr. Wind stress was applied at time $t = 12$ hr and continued, together with surface cooling, until the end of each simulation. Once the wind stress is applied, a new quasi-steady state should be reached at time $t_{ss-wind}$ after one half of the mode one internal wave period (e.g., Spiegel & Imberger, 1980). For an internal wave period of ≈ 7 hr, this should occur at $t_{ss-wind} \approx 16$ hr. Together with the zero wind stress case (run 0 in Table 1), we tested through a parametric study the effect of 6 different values of τ_w , increasing from $O(10^{-4})$ to (10^{-2}) N m⁻² which resulted in χ_{MO} values increasing from 0 to ≈ 0.5 (runs 1–6 in Table 1). The contribution of wind speed to the heat loss rate was not accounted for in these simulations, so the variability in χ_{MO} is only driven by changes in u_* .

To evaluate the effect of the wind alone and to test the “additive assumption”, that is, that the net transport can be expressed as a linear superposition of the wind- and thermally driven cross-shore transport, a set of 6 simulations (W-runs in Table 1) was conducted in which the lake was only forced with a surface wind stress. Details of the modeled flows for the W-runs and the resulting fit with the wind scaling (see Section 2.5) are included in Figure S1 in Supporting Information S1.

2.4. Calculation of Offshore Flows

Near-bed offshore flows were calculated, over time and for the entire basin, from the modeled width-averaged cross-shore velocity field as:

$$q_m(t, x) = \int_{z_1(t,x)}^{z_2(t,x)} u_c(t, x, z) dz. \quad (5)$$

Here u_c is the width-averaged cross-shore velocity. A positive u_c indicates an offshore directed current. Thus, $u_c = u_x$ in the upwind side ($x < L/2$, Figure 1a) and $u_c = -u_x$ in the downwind side ($x > L/2$, Figure 1a), where u_x is the width-averaged velocity field in the x -direction. z_1 and z_2 mark the limits of the integration over depth (Figures 1b–1e), which may vary over x and time. For the half of the lake located downwind, wind stress reinforces the convectively driven circulation and, as a result, a two-layered exchange flow develops in the littoral region. Depth z_1 is the shallowest stagnation depth within the water column, that is $u_c(t, x, z = z_1) = 0$ m s⁻¹.

Table 2
Key Geometric, Length and Flow Scales Used in This Study

Symbol	Definition	Value in runs 0–6	Units
$D(x)$	Lake bed depth	1–16	m
H	Lake maximum depth	16	m
h_{lit}	Average depth of each littoral region measured at profiles U and D.	5.44 ^a	m
h_{min}	Lake minimum depth	1	m
h_T	Thermocline depth	11.9 ^a	m
h_{SML}	Depth of the surface mixed layer	9.9 ^a	m
L	Length of domain	1,800	m
L_{SML}	Length of each littoral region: Cross-shore length where $D(x) = h_{SML}$.	297 ^a	m
q_c	Cooling-driven cross-shore unit-width discharge (Equation 1). Scaling	Figure 4a	$m^2 s^{-1}$
q_w	Wind-driven cross-shore unit-width discharge (Equation 7). Scaling	Figure 4a	$m^2 s^{-1}$
q_{total}	Total cross-shore unit-width discharge, $q_{total} = q_c + q_w$. Scaling	Figure 4a	$m^2 s^{-1}$
q_m	Modeled total offshore unit-width discharges (Equation 5)	Figure 4a	$m^2 s^{-1}$
S	Longitudinal slope	0.03	-
2δ	Metalimnion width	4 ^a	m
χ_{MO}	Non-dimensional Monin-Obukhov length scale (Equation 2).	Table 1	-

^aInitial values ($t = 0$).

Point z_2 is the depth of the lake bed at locations shallower than h_{SML} or, otherwise, the second stagnation depth from the lake surface (Figure 1c). For the other half of the lake, the upwind region, the cooling-driven circulation and wind-driven circulation act in opposite directions. If the wind is only able to slow down TSs, a three-layer exchange flow develops in the littoral region, with a surface (wind-driven) and near-bed (convectively driven) current directed offshore, and an intermediate onshore current (Figure 1d). Depths z_1 and z_2 are, in this case, the limits of the bottom convectively driven current, which correspond to the second and third (or the bottom of the lake at locations shallower than h_{SML}) stagnation depths from the surface, respectively.

We further use z_1 and z_2 to remove offshore circulation developing at the thermocline region, which is not the subject of this study. Specifically, z_1 should be shallower than h_{SML} and more than 2/3 of the layer should be above h_{SML} , that is $|h_{SML} - z_1| > 2/3 |z_2 - z_1|$. q_m is set to 0 $m^2 s^{-1}$ when this criterion is not met. If the wind-driven circulation overcomes the convectively driven circulation, a two-layer flow exchange develops in the littoral region, with a bottom current directed onshore, and thus $q_m = 0 m^2 s^{-1}$ (Figure 1e). As we are evaluating the effect of the wind on the intensity of TSs, q_m only includes the contribution of near-bed currents to offshore transport. In the downwind region, q_m is equal to the total offshore transport in the littoral region ($= 1/2 \int u_c |dz|$). In the upwind region, however, q_m is lower than the total offshore transport since we are not integrating the wind-driven near-surface currents (Figure 1d).

2.5. Combined Wind and Convective Cross-Shore Transport

In the proposed parameterization, we consider steady wind stress along the main axis of a lake and make the following assumptions: (a) vertical eddy viscosity, ν_z , is uniform within the SML and (b) slope effects are negligible (slope $S \ll 1$). We also recall the no-slip bottom boundary condition and flow continuity. Given such background conditions, the associated wind-driven steady-state velocity profile in the littoral region can be expressed as (e.g., Cormack et al., 1975):

$$u(x, z) = \frac{\tau_w}{\rho_0 \nu_z} \left(\frac{3}{4} \frac{(D(x) - z)^2}{D(x)} - \frac{D(x) - z}{2} \right), \quad (6)$$

where $D(x)$ is the maximum water column depth at a given x location within the littoral region (Figure 1a). The velocity profile in Equation 6 changes sign at a depth $z_0(x) = 1/3D(x)$. The wind-driven offshore flow, $q_w(x)$, can then be estimated by integrating Equation 6 from $z_0(x)$ to $D(x)$.

$$q_w(x) = \int_{z_0}^{D(x)} u(x, z) dz = \frac{\tau_w}{\rho_0 \nu_z} \frac{D(x)^2}{27}. \quad (7)$$

Thus, within the littoral region, q_w is maximal at its offshore end, where $D(x) = h_{\text{SML}}$. The value of the vertical eddy viscosity was selected from the modeled results in the W-runs. Modeled offshore unit-width discharges in the W-runs were fit to Equation 7 to obtain an average SML viscosity that is representative for all runs (Figure S1 in Supporting Information S1). The good fit between modeled and estimated (Equation 7) wind-driven unit-width discharges supports that the selection of a single value for ν_z is indeed reasonable for the range of low to mild winds tested in this study.

We assume that net cross-shore transport can be expressed as a linear superposition of surface cooling and wind effects. The validity of this linear assumption is tested and discussed in Section 3.3. Therefore, offshore discharge per unit width is estimated as:

$$q_{\text{total}} = q_c + q_w, \quad (8)$$

where q_c is defined in Equation 1 and q_w is positive (directed offshore) at depths deeper than $z_0(x)$ on the side where the wind blows toward the littoral. Since we are interested in the discharge transported by offshore bottom currents, we will set $q_{\text{total}} = 0 \text{ m}^2 \text{ s}^{-1}$ whenever $(q_c + q_w) < 0 \text{ m}^2 \text{ s}^{-1}$. The latter occurs when the wind-driven circulation overcomes the convectively driven circulation in the upwind littoral region (Figure 1e).

The different expressions for the flow scaling (q_c , q_w , and q_{total}) were compared with the modeled flows, q_m (Equation 5) in profiles U and D (Figure 1a) during the quasi-steady-state period ($t > t_{\text{ss-wind}}$, see Section 2.3). These profiles are located at the initial offshore end of the upwind and downwind littoral regions, respectively. Given that those are fixed profiles, the vertical length scales in the calculations of q_c and q_w are kept constant. For computing the convective scaling (Equation 1), $h_{\text{lit}} = h_{\text{lit},0}$, which is the average depth of the initial mixed littoral region. For the wind scaling (Equation 7), $D = h_{\text{SML},0}$, which is the initial SML depth. The forcing length scale, L_{SML} , however, grows as the SML deepens over time (e.g., Doda et al., 2022).

3. Results

3.1. Upwind and Downwind Lake Circulation

Figure 2 shows the cross-shore velocity profiles at U and D locations for $t > t_{\text{ss-wind}}$, once a quasi-steady state is reached after wind stress is applied. The characteristic cross-shore circulation cell associated with TSs in the littoral region of a lake is observed for the runs with the smallest χ_{MO} values ($\chi_{\text{MO}} = 0$ and $\chi_{\text{MO}} = \text{O}(10^{-3})$ in Figures 2a and 2b). Density currents flow downslope, leading to positive cross-shore velocities near the littoral bed. A return flow, with negative cross-shore velocities, develops in the upper part of the water column to fulfill continuity. This characteristic velocity profile is observed in both littoral regions (blue and red lines in Figures 2a and 2b). As χ_{MO} increases, and reaches magnitudes above $\text{O}(10^{-2})$, TSs in the upwind side tend to be arrested, as shown by the decreasing near-bed cross-shore velocities (red lines in Figure 2c). For $\chi_{\text{MO}} \gtrsim 0.07$ ($\tau_w \gtrsim 0.0058 \text{ N m}^{-2}$, $u_{10} \gtrsim 1 \text{ m s}^{-1}$) our simulations already predict a reversed circulation in the upwind side, with bottom currents directed onshore ($u_c < 0 \text{ m s}^{-1}$ in Figures 2d–2g). By contrast, the cross-shore exchange is amplified in the downwind littoral region since the wind and thermally driven circulation work in phase, resulting in an enhancement of near-bed currents (blue lines in Figures 2c–2g). The depth where the velocity profile changes sign also becomes shallower as χ_{MO} (and so wind stress) increases. For the two simulations with the highest χ_{MO} , this depth approaches the value of $z_0 (= 1/3D(x); \approx 3.3 \text{ m}$ in Figure 2g) predicted by Equation 3 (see Section 2.2), suggesting that the wind was the predominant flow driver.

3.2. Flow Discharges From the Littoral Region

Wind-driven changes in the circulation pattern reported in Section 3.1 impacted the near-bed transport of littoral water toward the lake interior (Figure 3). For the zero wind-stress case ($\chi_{\text{MO}} = 0$), there is bilateral symmetry in

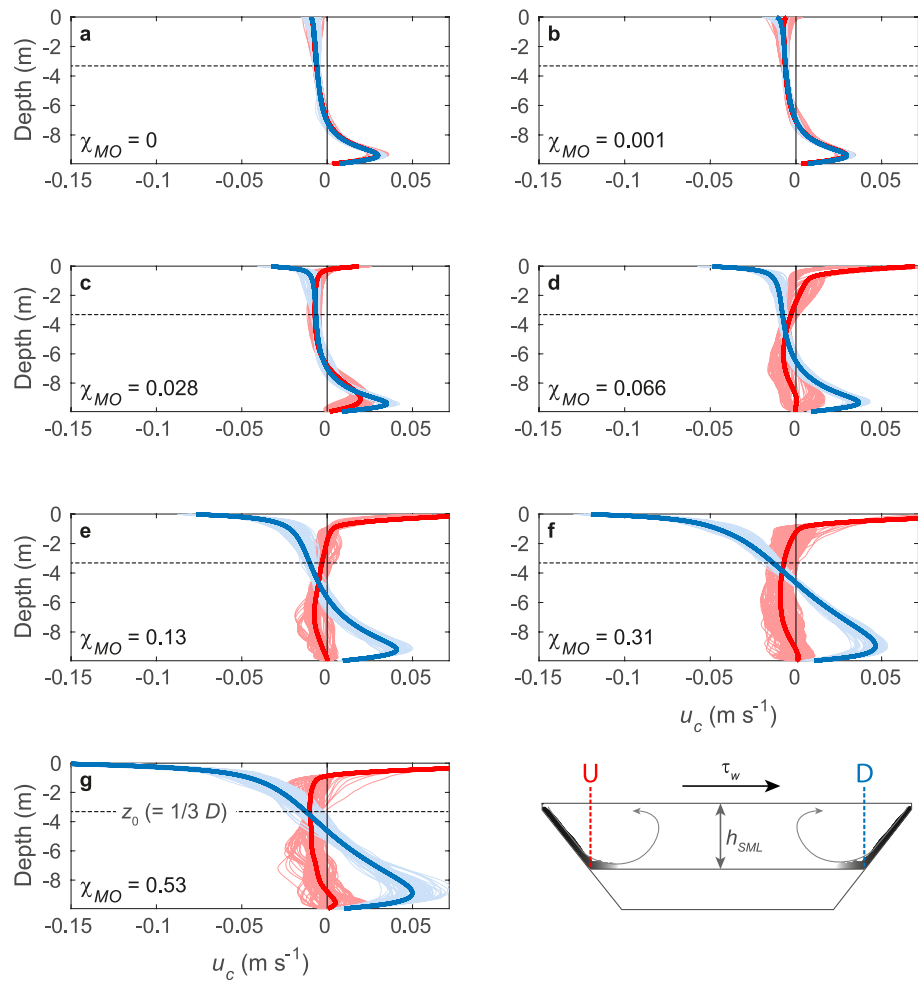


Figure 2. Velocity profiles in the upwind and downwind littoral regions during the quasi-steady period ($t > t_{ss-wind}$). Instantaneous (light colors) and time-averaged (thick lines) cross-shore velocity profiles in the (red) upwind and (blue) downwind littoral regions at locations where $D(x) = 9.9$ m (locations U and D, respectively), for runs 0–6 in Table 1. Velocity is positive if directed offshore.

the q_m signal (Figure 3a). On each sloping side, the maximum flow rate is observed near the end of the littoral region (red dotted lines in Figure 3), and from there, it decreases both toward the lateral boundaries and the lake center. Once wind stress is applied over the lake ($\chi_{MO} > 0$ for $t \geq 12$ hr), the upwind side experiences two main modifications. First, the area with near-bottom offshore discharge ($q_m > 0$ m² s⁻¹) decreases (e.g., Figure 3c). Second, the location of the maximum flow rate is displaced offshore (e.g., Figures 3d and 3e). These two effects are intensified as the magnitude of the wind stress increases, especially the reduction of q_m (Figures 3f and 3g). In the downwind region, the area with $q_m > 0$ m² s⁻¹ expands toward the lake interior as the stress increases. Still, maximum values remain centered around the end of the littoral region (Figures 3a–3f), except for the strongest wind (Figure 3g).

As the magnitude of the applied wind stress increases, the magnitude of the near-bed offshore flow increases (decreases) with respect to the wind-free case in the downwind (upwind) region (Figure 3). These trends are shown in the time series of q_m at locations U and D (Figure 4). Downwind, modeled flows subjected to the highest wind stress rapidly increased to values that quadruple on average those in the wind-free case. Upwind, the modeled flow rapidly decreased and represents, for $\chi_{MO} \gtrsim 0.07$, less than 20% of the flow in the wind-free case.

Light blue and red lines in Figure 2 show that, within this quasi-steady state, the velocity profiles still show time variability around mean values. This variability is also displayed in the cross-shore unit-width discharges (Figures 3 and 4a–4b). Ulloa et al. (2022) show that the cross-shore transport—within the quasi-steady state

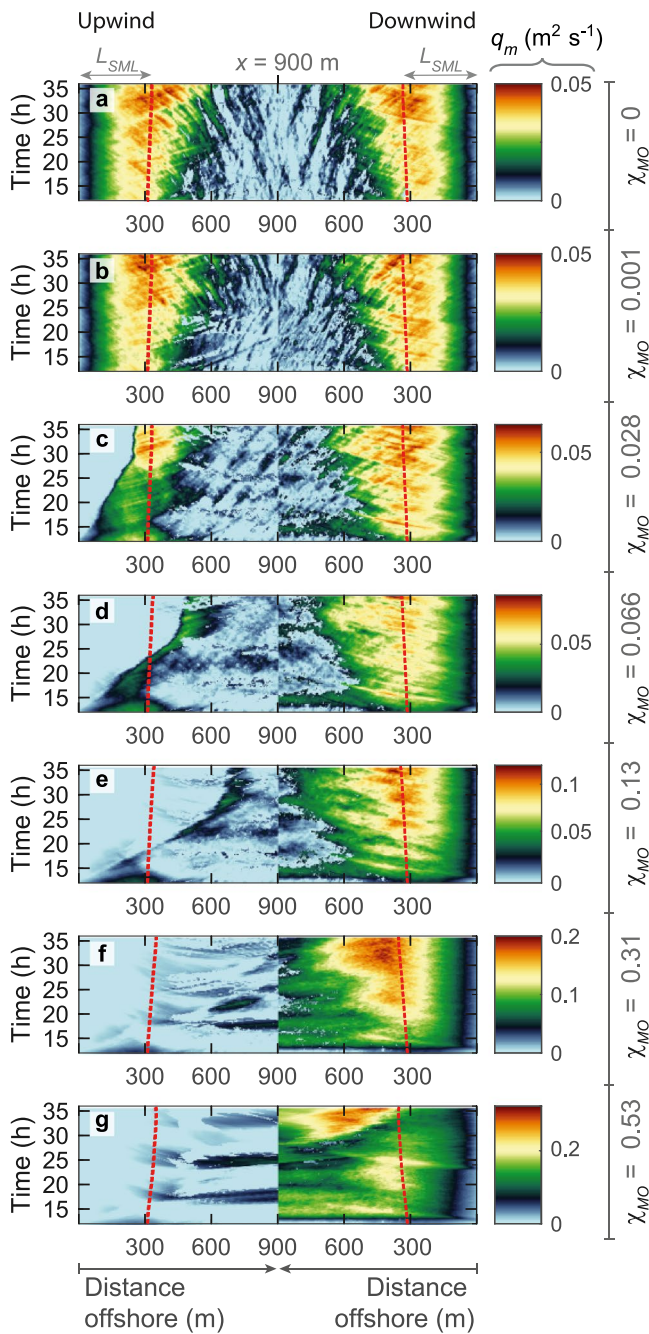


Figure 3. Space-time modeled bottom offshore unit-width discharges, q_m , for different χ_{MO} . Results of (a–g) runs 0–6 in Table 1. Offshore discharges are positive if directed toward the lake center, located at $x = 900$ m, where the offshore direction reverses. As χ_{MO} increases, the basin-scale wind circulation dominates over the convective circulation, and bottom offshore discharges are restricted to the downwind region. Red lines show the 6h-smoothed end of both littoral regions calculated from an equilibrium density profile where density is redistributed to attain the minimum potential energy in the system (Winters et al., 1995). Wind stress over the lake starts at $t = 12$ hr. Note the increasing range of the colorbar from (a) to (g).

regime—may exhibit significant time variability due to the interaction of TSS with convective plumes, especially in the sloping zone close to the interior stratified region where baroclinic oscillations are energized both by thermal siphons and convective plumes. In the lake interior, time variability is also affected by internal waves triggered by the intrusion of density currents at the base of the SML (see also Ulloa et al., 2019). The interaction of convective and wind-driven currents also introduced unsteadiness in the velocity and flow signals. See, for example, the low-frequency oscillations in q_m in the downwind and upwind profiles in Figure 4 for the largest χ_{MO} . The nature of these oscillations is beyond the scope of this study and hereon we will focus on the time-averaged cross-shore transport.

3.3. Parameterization of Discharge From the Littoral Region

The model results confirm that the wind can either enhance or block TSS. This section illustrates that the assumption of linearity between convectively and wind-driven effects on the cross-shore exchange is reasonable over the studied χ_{MO} range. Figure 5a shows the time-averaged modeled flows in profiles U and D (red open and closed squares, respectively) together with the results from the three different scalings. Recall that there is a proportionality coefficient, a , in the convective flow scaling (Equation 1) and that vertical viscosity, ν_z , appears in the scaling for the wind-driven discharge (Equation 7). The linear assumption implies that the values of both a and ν_z are independent of the applied wind stress, and thus, that one unique value should be used for the parameter space here examined.

The value of a was obtained by fitting Equation 1 to the modeled flows for the wind-free case, which results in $a = 0.29 \pm 0.01$. This value is within the expected range predicted in the laboratory experiments of Harashima and Watanabe (1986) although lower than their empirical relationship $a \approx 0.43 - 1.67/Re_f^{1/2}$, where $Re_f (= B_0^{1/3} h_{lit}^2 L_{SML}^{-2/3} \nu^{-1})$ is the flux Reynolds number and $\nu \approx 1.2 \times 10^{-6} \text{ m}^2 \text{ s}^{-1}$ the kinematic viscosity of water. For $Re_f \approx 1,700$, a should be ≈ 0.39 and q_c 30% higher. A 30% uncertainty in q_c is within the range of sensitivity of the modeled q_c to the selected value of background horizontal viscosities (see Supporting Information S1). Moreover, Harashima and Watanabe (1986) imposed a localized destabilizing heat flux over a flat shallow water shelf that joined a deeper reservoir without a sloping region. Both the spatial distribution of the destabilizing heat flux and the shape of the littoral region differ from those in this study. The time-averaged discharge q_c , predicted using Equation 1, is shown as a function of χ_{MO} in black in Figure 5a; q_c remains almost constant through the range of χ_{MO} . The latter was expected given a maximum difference in the deepening of the SML during the time-averaging period of only 0.5 m between simulations. With a longitudinal slope S of 0.03, this deepening resulted in an increase of L_{SML} of ≈ 20 m. Since q_c is a function of the length of the littoral region to the power of $1/3$, differences in the rate of SML deepening among simulations could only introduce $O(10^{-3}) \text{ m}^2 \text{ s}^{-1}$ differences in the estimated convective flows during the time-averaging period.

The value of ν_z was obtained by fitting Equation 7 to the modeled flows in the downwind littoral region in the simulations where the lake surface was only subjected to wind stress (W-simulations, in Table 1). This fit leads to a value for ν_z of $6.0 \pm 0.4 \times 10^{-4} \text{ m}^2 \text{ s}^{-1}$ (see Figure S1 in Supporting Information S1). This value of ν_z is of the same order of magnitude of the modeled viscosities within the SML (Figure S2 in Supporting Information S1) and

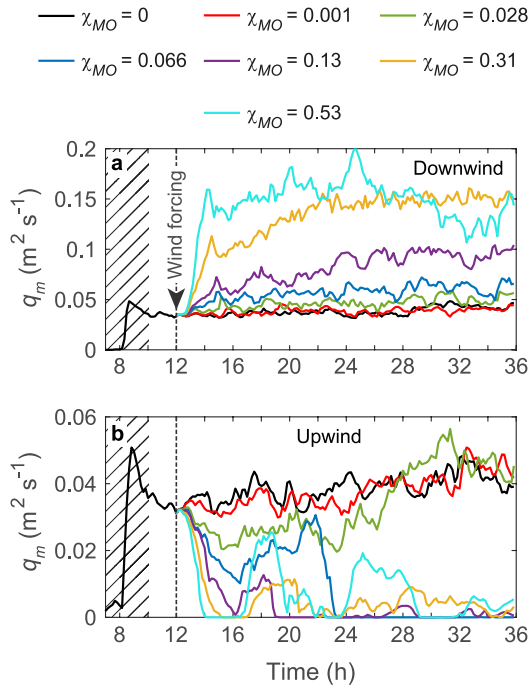


Figure 4. Time series of modeled flows for different χ_{MO} . Profiles (a) D (downwind) and (b) U (upwind). Gray oblique lines mark the TS-development period. Wind stress over the lake starts at $t = 12$ hr.

of the same order of magnitude as measured vertical viscosities in lake and oceanic SMLs for the same range of wind stresses (e.g., Bengtsson, 1973; Santiago-Mandujano & Firing, 1990). The low uncertainty at 95% confidence interval for ν_z supports the use of the linear assumption within the range of low wind stresses tested in this study. Equation 7 predicts a linear increase of the wind-driven offshore flows in the downwind littoral region as χ_{MO} and the applied stress increases, as indicated by the blue line in Figure 5a. Given that q_c remained almost constant among simulations, the addition of convectively and wind-driven effects in the downwind region (closed light blue circles in Figure 5a) is reflected as an offset to the discharges predicted by Equation 7. In the upwind region, on the other hand, the subtraction of the two effects predicts reversed flows, $q_{total} = 0 \text{ m}^2 \text{ s}^{-1}$, for $\chi_{MO} \gtrsim 0.1$ ($\tau_w \geq 9 \times 10^{-3} \text{ N m}^{-2}$, open light blue circles).

While the interaction of TS and wind-driven currents is fundamentally a nonlinear problem, our simple linear approach has useful predicting skills (Figures 5b and 5c). Upwind trends are correctly reproduced. Given the small magnitude of the flows, deviations are higher than on the downwind side and become 100% as χ_{MO} increases and the scaling predicts reversed flows ($q_c + q_w = 0$). On the downwind side, in our worst-case scenario, the deviation between modeled and predicted flows remained <27% (Figure 5b).

4. Discussion

Our model results show that mild winds are able to interact with TSs and that the resultant offshore unit-width discharges can be predicted by the proposed practical mathematical expression in Equation 8. In this section, we will

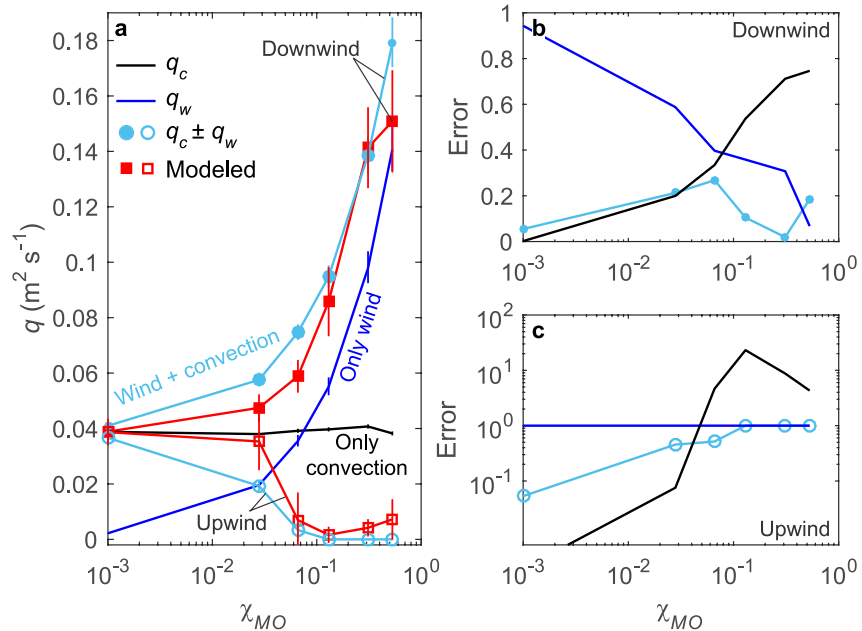


Figure 5. Modeled vs. predicted flows for different χ_{MO} . (a) Time-averaged predictions with the convective (black), wind-driven (dark blue), and additive (linear) scaling (light blue) vs. modeled (red) flows in profiles U (upwind, open symbols) and D (downwind, closed symbols). The time-averaging period is $t = 16\text{--}36$ hr when $t > t_{ss-wind}$. Vertical lines on the modeled values show \pm one standard deviation. Vertical lines in the different scaling curves show the uncertainty coming from the 95% confidence interval of the fitting coefficient $a (= 0.29 \pm 0.006)$ in Equation 1 and $\nu_z = 6.06 \times 10^{-4} \pm 3.6 \times 10^{-5} \text{ m}^2 \text{ s}^{-1}$ in Equation 7. (b–c) Non-dimensional error for the different scaling predictions in (a). Relative error = $|q_m - q_\beta|/q_m$, where q_β refers to any of the tested scalings (q_c , q_w , and q_{total}). Upwind, once $q_\beta = 0$, the relative error becomes 100%.

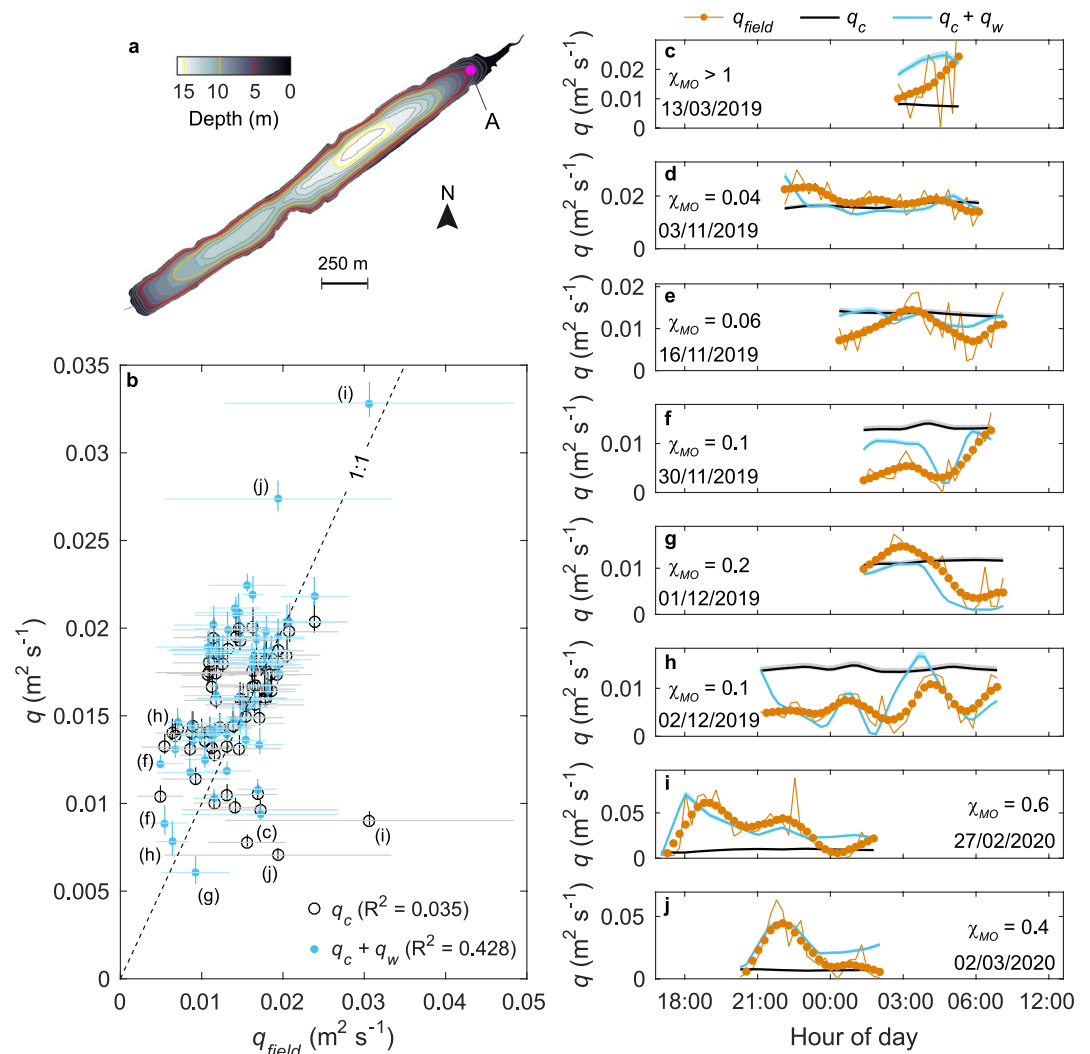


Figure 6. Predicted vs. measured unit-width discharges during cooling periods in Rotsee. (a) Bathymetry of Rotsee indicating the measurement location (point A). (b) 1:1 relationship of daily averages of measured (q_{field}) and predicted unit-width discharges for the convective scaling (q_c , Equation 1) and the additive (linear) scaling for wind and convection ($q_c + q_w$, Equation 8) for 66 days in Rotsee. Discharges were averaged over each daily cooling period. Vertical and horizontal lines crossing the open and closed circles show the 95% confidence interval of proportionality coefficient a ($= 0.34 \pm 0.02$; Doda et al., 2022) and ν_z ($= 6.06 \times 10^{-4} \pm 3.6 \times 10^{-5} \text{ m}^2 \text{ s}^{-1}$, see Supporting Information S1) and ± 1 standard deviations of q_{field} , respectively. (c–j) Example of measured and predicted unit-width discharges and average χ_{MO} during eight different flushing events in Rotsee. Letters beside some of the symbols in (b) correspond to the cooling periods shown in panels (c–j). A 3h-smoothing (filled orange circles) was applied to all the unit-width discharge signals.

confirm its applicability by testing it in Lake Rotsee, a small and shallow Swiss lake from which long-term data on TSS, and specifically on unit-width discharges, is available (Doda et al., 2022). Our interaction regime, defined on the basis of χ_{MO} will be put in the context of previous formulations defining the relative magnitude of shear and buoyancy forces in lake and coastal littoral regions. Finally, we will discuss the broader applicability framework of the proposed scaling.

4.1. Field Application: Lake Rotsee

Rotsee (47.06°N, 8.31°E and maximum depth of 16 m, Figure 6a) is a Swiss dimictic perialpine elongated lake. Doda et al. (2022) studied the seasonal occurrence of TSS in this lake. By deploying a chain of thermistors and an upward-looking acoustic Doppler current profiler in the north-eastern littoral region of the lake (point A in Figure 6a) during a year-long field study, they were able to detect the presence of TSS (see details of field

measurements and TS detection procedure in Doda et al., 2022). The authors obtained a value for the proportionality coefficient $a = 0.34 \pm 0.02$ (Equation 1) yet highly scattered ($R^2 = 0.27$). The lake is characterized by its calm conditions; still, cross-shore flows were identified as wind-driven for almost 10% of the days with measurements (Doda et al., 2022). We applied our framework to the days with cross-shore flows identified as TSs or wind-driven flows by Doda et al. (2022). We further restrict our study to night-time flushing events, when radiative forcing is zero. We calculated q_c with the proportionality coefficient established by Doda et al. (2022) and set the littoral depth $h_{lit} = 1.7$ m (the average depth of the littoral region onshore of point A). We calculated q_w using the lake depth at the measured location, $D = 4.2$ m (point A, Figure 6a). B_0 during the cooling periods was on average $O(10^{-8})$ W kg⁻¹, with an $O(10^{-9}$ – $10^{-7})$ W kg⁻¹ range. τ_w ranged from $O(10^{-8})$ to $O(10^{-2})$ N m⁻². Due to the progressive deepening of the surface mixed layer, L_{SML} increased from ≈ 200 m in June to ≈ 800 m in December (Doda et al., 2022).

By adding days with cross-shore flows defined as wind-driven by Doda et al. (2022), predicted unit-width discharges further deviate from the 1:1 relationship with the convective scaling, q_c , and $R^2 < 0.1$ (black open circles in Figure 6b). Examples of such wind-driven events are shown in Figures 6c, 6i, and 6j, where the convective scaling (black lines) fails to predict the magnitude of the measured (orange signal) offshore discharges. Predicted offshore discharges including the effect of the wind in the scaling (blue lines) closely follow the measured ones on those same days. Other examples of days when TSs interacted with wind-driven currents are shown in Figures 6d–6h. For example, Figures 6f and 6h show days when the wind forcing effectively weakened TSs. Overall, including wind effects increased the goodness of predictions for unit-width discharges in the littoral region in Rotsee ($R^2 = 0.43$, Figure 6b).

4.2. The Interaction Regime

A non-dimensional Monin-Obukhov length scale has been used in this study to define the interaction regime between convection and wind in the flushing of lakes' littoral regions. Our results indicate that this regime occurs for values of χ_{MO} in the range $0.1 \lesssim \chi_{MO} \lesssim 0.5$. Indeed, for this range of χ_{MO} , unit-width discharges are better predicted in our simulations and Lake Rotsee (Figure 6) when both the wind- and convectively driven transport scalings are included (Equation 5, Figure 5). Rueda et al. (2007) reported that offshore winds of 3 m s⁻¹ were able to weaken TSs in La Caldera (37°N, 3°W). For $B_0 \approx 7 \times 10^{-8}$ W kg⁻¹ and $h_{SML} \approx 10$ m during their simulated period (calculated from reported w_* and h_{SML} values in Rueda et al., 2007), a 3 m s⁻¹ wind results in $\chi_{MO} \approx 0.1$. Sturman et al. (1999) reported evidence of TSs in well-mixed 3-m-deep Lake Yangebup (32°S, 115°E) when winds were below 3 m s⁻¹. For $h_{SML} \approx 3$ m (well-mixed lake), and their reported values of heat loss rate of ≈ 200 W m⁻² ($B_0 \approx 8 \times 10^{-8}$ W kg⁻¹); the latter scenario corresponds to $\chi_{MO} \lesssim 0.4$. Both examples are consistent with our defined interaction regime based on χ_{MO} .

Other parameters have been suggested in the literature to evaluate the interaction between wind- and density-driven flows. For example, studies on cross-shore exchanges due to differential cooling in the inner shelves of oceanic coastal waters commonly use the horizontal Richardson number, Ri_x (e.g., Horwitz & Lentz, 2014; Mahjabin et al., 2019, 2020):

$$Ri_x = \frac{g D(x)^2}{\rho_0 u_*^2} \frac{\partial \rho}{\partial x}, \quad (9)$$

where $\partial \rho / \partial x$ is the cross-shelf density gradient. The horizontal Richardson number (Equation 9) is inversely proportional to χ_{MO} (Equation 2). For a shear time scale, $t_{shear} \sim L_{SML} k u_*^{-1}$, and in the absence of horizontal advection of heat, the horizontal density gradient built by differentially cooling over the wedge region will increase up to (e.g., Horwitz & Lentz, 2014):

$$\frac{\partial \rho}{\partial x} = -\frac{B_0 \rho_0}{g} \frac{S}{D(x)^2} t_{shear} \approx -\frac{B_0 \rho_0 h_{SML} k}{g u_*} \frac{1}{D(x)^2}, \quad (10)$$

where the cross-shore slope $S \approx h_{SML} / L_{SML}$. Note that from Equation 10, it yields that $\chi_{MO} \approx Ri_x^{-1}$. Our simulations confirm indeed this approximate relationship (see Figure S3 in Supporting Information S1).

Horwitz and Lentz (2014) explored through numerical simulations the effect of the presence of a horizontal density gradient on the circulation driven by cross-shore directed winds. For absolute values of $|Ri_x| < 1$ ($|\chi_{MO}| > 1$),

they showed that the main effect of the presence of a horizontal density gradient is to enhance or decrease vertical shear by strengthening vertical stratification or destabilizing the water column, respectively. For $Ri_x > 1$ ($\chi_{MO} < 1$), however, Horwitz and Lentz (2014) hypothesized that the horizontal density gradient had an increasing contribution in directly driving the cross-shore circulation. This was eventually confirmed by Mahjabin et al. (2019) in their field experiments in the Rottneest continental shelf (32°S, 115°E, Australia), where they observed that strong thermally driven dense shelf water cascades develop when $Ri_x \gtrsim 2$ ($\chi_{MO} \lesssim 0.5$).

Woodward et al. (2017) applied in their numerical simulations of the hydrodynamics of Lake Argyle (16°S, 128°E) the parameter B introduced by Cormack et al. (1975) to measure the relative magnitude of shear and buoyancy forces in shallow rectangular cavities with differentially heated end-walls:

$$B = \frac{L\tau_w}{h^2\Delta T\alpha g} . \quad (11)$$

Here, L and h correspond to the length and depth of the cavity, respectively, and ΔT is the temperature difference between the differentially heated end-walls. Applying the latter scaling to the littoral region of lakes with $S \ll 1$ and assuming a constant horizontal density gradient $\partial\rho/\partial x \sim \rho_0\alpha\Delta T L^{-1}$, expression (Equation 11) reduces to $B \approx \chi_{MO} \approx Ri_x^{-1}$. Woodward et al. (2017) reported that for values of $0.1 \lesssim B \lesssim 0.5$, the cross-shore exchange was driven by a combination of wind and horizontal convection, while for values of $B \lesssim 0.1$ and $B \gtrsim 0.5$, the exchange was mainly driven by convection and wind shear, respectively. Given that $B \approx \chi_{MO}$, this regime delimitation is consistent with our simulations. The upper and lower bounds of the interaction regime are however approximate, given the dependency of the convective velocity on the longitudinal slope ($\sim S^{-1/2}$). The validity of parameter χ_{MO} as a regime delimiter is nontrivial. χ_{MO} does not include information on the horizontal density gradient between the littoral and interior regions and could thus be calculated based on the forcing conditions (B_0 , u_*) and h_{SML} . This is the advantage of using χ_{MO} since the latter information can simply be inferred from one single mooring deployed in a lake.

4.3. Applicability Framework

The mathematical expression in Equation 8 is expected to work as long as (a) (quasi-)steady conditions are reached, (b) wind stress and convection are the main sources of turbulence and water motions in the lake, and (c) Coriolis effects are negligible. The scaling for buoyancy-driven horizontal transport introduced in Equation 1 already assumes a steady thermal equilibrium and an equilibrium between the inertial advective term and the pressure gradient term in the cross-shore momentum balance, that is:

$$u \frac{\partial \bar{T}}{\partial x} \approx \frac{Q_o}{\rho_0 c_p D(x)} , \quad (12)$$

$$u \frac{\partial u}{\partial x} \approx \frac{1}{\rho_0} \frac{\partial p}{\partial x} , \quad (13)$$

where p ($\approx \alpha g \rho_0 \bar{T} D(x)$) is pressure and \bar{T} is a depth-averaged temperature. Monismith et al. (2006) studied the exchange flows due to differential cooling in a coral reef in the Red Sea. They showed, by nondimensionalizing the governing momentum and buoyancy equations, that neglecting the unsteady/inertial term $\partial u/\partial t$ is a reasonable assumption as long as $(h_{SML} S^{-2/3} P^{-1} w_*^{-1}) \ll 1$, P being the period of the thermal forcing (heating/cooling cycle). In our simulations, where a constant cooling rate is applied ($P \rightarrow \infty$), this condition is met. In Rotsee, at the time when TSs were observed (July–December), h_{SML} ranged from 2 to 16 m, and average w_* from 5×10^{-3} to 6.5×10^{-3} m s⁻¹ (Doda et al., 2022). For $S = 0.03$ and a 24 hr cooling cycle, the term $(h_{SML} S^{-2/3} P^{-1} w_*^{-1})$ remained always < 0.4 and Doda et al. (2022) showed that Equation 1 successfully predicted cross-shore flows in the lake during TS events. However, this condition may not be met in deeper littoral regions, with lower slopes, lower surface buoyancy fluxes, and/or shorter cooling periods (e.g., Molina et al., 2014), where flow dynamics may follow an inertial-viscous buoyancy balance (e.g., Farrow, 2013; Farrow & Patterson, 1993; Lin, 2015; Ulloa et al., 2018).

In this study, the viscous term contributes to the exchange flows once wind stress acts on the lake surface. However, strong background currents (e.g., alongshore currents, Ulloa et al., 2018) and/or high bed roughness, for example, could also contribute to this term. In our scaling, we also consider that mild winds do not lead to

strong tilting of the isotherms. Assuming a two-layer stratified system, the expected displacement $\Delta h/h_T$ can be estimated from the Wedderburn number W as (Shintani et al., 2010) $\Delta h/h_T = 1 - [2\pi^{-1} \tan^{-1}(9/8 W - 1)]^{0.57}$, where $W = g'h_T^2 u_*^{-2} L^{-1}$, and $g' (= g(\rho_2 - \rho_1)\rho_2^{-1})$ is the reduced gravity calculated with the bottom-layer (ρ_2) and top-layer (ρ_1) densities. Thus, mild winds could still lead to upwelling events in long lakes (large L) with shallow thermoclines (small h_T) and/or weak stratification (small g'). The balance between the cross-shore barotropic pressure gradient and viscous terms, from which we derive an expression for q_w , is expected to work in shallow elongated basins where H is $O(10)$ m and the dynamics of the littoral region can be studied in a 2-D x - z framework.

Background stratification affects the development of TSs in a two-fold way. First, it affects the forcing conditions, through changes in the buoyancy flux and the geometry of the littoral region. For a given surface cooling heat flux, the SML temperature will dictate the value of the thermal expansivity α , and thus the magnitude of the buoyancy flux B_0 . For example, Doda et al. (2022) reported that in Rotsee, the surface heat flux decreases from summer to winter, however, the strong seasonal variability of B_0 (one order of magnitude larger in summer than in winter) is mainly due to seasonal changes in α . The depth of the SML also affects the initial length L_{SML} and the average depth h_{lit} of the littoral region (e.g., Figure 1a), modifying the magnitude of TS velocities and unit-width discharges (Equation 1). Second, for a given B_0 , the depth of the SML h_{SML} and the strength of the background stratification dictates the deepening rate of the seasonal SML. The convective deepening rate of the SML can be expressed as (Zilitinkevich, 1991):

$$\frac{dh_{SML}}{dt} = (1 + 2A) \frac{B_0}{h_{SML} N^2}. \quad (14)$$

Here N is the buoyancy frequency below the SML ($N^2 = -g\rho_0^{-1}\partial\rho/\partial z$), and $A \approx 0.2$ (Zilitinkevich, 1991) is an empirical entrainment coefficient. Once the wind acts over the lake, its contribution to the deepening rate of the SML increases as L_{MO} increases, and the deepening rate of the SML should then be parameterized as a function of both convection and wind forcing (Batchvarova & Gryning, 1991; Driedonks, 1982):

$$\frac{dh_{SML}}{dt} = \frac{(1 + 2A)w_*^3 + Bu_*^3}{h_{SML}^2 N^2}, \quad (15)$$

where $B \approx 0.25$ (Batchvarova & Gryning, 1991) is an empirical constant accounting for shear entrainment. Using Equation 2, Equation 15 can be expressed as:

$$\frac{dh_{SML}}{dt} = \frac{B_0}{h_{SML} N^2} (1 + 2A + B\chi_{MO}k) \approx \frac{B_0}{h_{SML} N^2} (1.4 + 0.1025\chi_{MO}) \quad (16)$$

In our simulations, the maximum χ_{MO} is 0.53 which indicates that wind forcing is only responsible for an increase of the deepening rate of less than 4%. Neglecting the effect of wind forcing, and assuming constant B_0 and constant N^2 below the SML, the expected deepening of the SML, Δh_{SML} , during a cooling period Δt_c would be:

$$\Delta h_{SML} = \left(\frac{2(1 + 2A)B_0}{N^2} \Delta t_c + h_{SML,0}^2 \right)^{1/2} - h_{SML,0} \quad (17)$$

For a constant longitudinal slope and fixed measuring profiles (i.e., $h_{lit} = h_{lit,0}$ in Equation 1 and $D = h_{SML,0}$ in Equation 7) the deepening Δh_{SML} would result in a negligible change in q_w , but in increasing values of q_c over the cooling period. The maximum increase of q_c is $(L_{SML,0} + \Delta h_{SML} S^{-1})^{1/3} L_{SML,0}^{-1/3}$. Thus, even if the forcing conditions (B_0, τ_w) remain steady throughout a cooling period, quasi-steady-state conditions may not be reached in lakes with weak background stratification (low N^2) and small longitudinal slopes (large $\Delta h_{SML} S^{-1}$).

For a Coriolis frequency $f \approx 1.1 \times 10^{-4} \text{ s}^{-1}$ as in Rotsee and maximum offshore cross-shore velocities u_{c-max} of 0.03 m s^{-1} for the zero wind stress case (Figure 2), the Rossby number in our simulations, $Ro = u_{c-max} (f L_{SML})^{-1}$, is ≈ 1 and Coriolis acceleration should not affect the trajectories of the downslope density currents before intruding at the base of the mixed layer. Moreover, we tested the interaction of TS with cross-shore winds, so that wind-driven currents do not contribute to the Coriolis-acceleration term, νf , in the cross-shore momentum equation. Studies in lake and oceanic littoral regions have shown, however, that strong alongshore tidally driven (Ulloa

et al., 2018) or wind-driven currents (e.g., Jabbari et al., 2019; Lentz & Fewings, 2012; Wu et al., 2018) could also affect cross-shore flows via Coriolis acceleration.

5. Conclusions

The mechanisms responsible for cross-shore exchanges between the littoral and pelagic region of lakes have been traditionally investigated separately even though most of the time lake dynamics result from a combination of different forcings. This study takes a step in that direction by analyzing the effect of the interaction of differential cooling and wind-driven currents on cross-shore discharges within the surface mixed layer of enclosed stratified basins. We have proposed a practical mathematical expression of the form $q_{\text{total}} = q_c + q_w$ that accounts for the cooling- (q_c) and wind-driven (q_w) contributions for the net cross-shore discharge. This expression is shown to improve cross-shore discharge predictions in the littoral region of lakes with negligible alongshore currents and under (quasi-)steady forcing conditions and cross-shore directed winds. We suggest using this parameterization in a well-defined range of non-dimensional Monin Obukhov length scale $0.1 \lesssim \chi_{\text{MO}} \lesssim 0.5$.

Data Availability Statement

MITgcm input files used in this study and data displayed in the figures can be accessed at <https://doi.org/10.5281/zenodo.6200351>.

Acknowledgments

This work was supported by the Swiss National Science Foundation (project Buoyancy driven nearshore transport in lakes, HYPOLimnetic THERmal SlphonS, HYPOTHESIS, reference 175919). Computer resources were provided by the Swiss National Supercomputing Centre and the IT and Communications Centre (CSIRC) of the University of Granada. The authors thank the two anonymous reviewers for their thorough comments and suggestions. Open access funding provided by ETH-Bereich Forschungsanstalten.

References

- Batchvarova, E., & Gryning, S. E. (1991). Applied model for the growth of the daytime mixed layer. *Boundary-Layer Meteorology*, 56(3), 261–274. <https://doi.org/10.1007/BF00120423>
- Bengtsson, L. (1973). Conclusions about turbulent exchange coefficients from model studies. *Hydrological Sciences Journal/Journal Des Sciences Hydrologiques*, 109(1), 306–312.
- Bengtsson, L. (1978). Wind induced circulation in lakes. *Hydrology Research*, 9(2), 75–94. <https://doi.org/10.2166/nh.1978.0007>
- Biemond, B., Amadori, M., Toffolon, M., Piccolroaz, S., Van Haren, H., & Dijkstra, H. A. (2021). Deep-mixing and deep-cooling events in Lake Garda: Simulation and mechanisms. *Journal of Limnology*, 80(2). <https://doi.org/10.4081/jlimnol.2021.2010>
- Biton, E., Silverman, J., & Gildor, H. (2008). Observations and modeling of a pulsating density current. *Geophysical Research Letters*, 35(14), L14603. <https://doi.org/10.1029/2008GL034123>
- Bonvin, F., Rutler, R., Chavre, N., Halder, J., & Kohn, T. (2011). Spatial and temporal presence of a wastewater-derived micropollutant plume in Lake Geneva. *Environmental Science and Technology*, 45(11), 4702–4709. <https://doi.org/10.1021/es2003588>
- Carpenter, S. R., Caraco, N. F., Correll, D. L., Howarth, R. W., Sharpley, A. N., & Smith, V. H. (1998). Nonpoint pollution of surface waters with phosphorus and nitrogen. *Ecological Applications*, 8(3), 559–568. [https://doi.org/10.1890/1051-0761\(1998\)008\[0559:NPOSWW\]2.0.CO;2](https://doi.org/10.1890/1051-0761(1998)008[0559:NPOSWW]2.0.CO;2)
- Coman, M. A., & Wells, M. G. (2012). An oscillating bottom boundary layer connects the littoral and pelagic regions of Lake Opeongo, Canada. *Water Quality Research Journal of Canada*, 47(3–4), 215–226. <https://doi.org/10.2166/wqrj.2012.039>
- Cormack, D. E., Stone, G. P., & Leal, L. G. (1975). The effect of upper surface conditions on convection in a shallow cavity with differentially heated end-walls. *International Journal of Heat and Mass Transfer*, 18(5), 635–648. [https://doi.org/10.1016/0017-9310\(75\)90275-6](https://doi.org/10.1016/0017-9310(75)90275-6)
- Cortés, A., Fleenor, W. E., Wells, M. G., de Vicente, I., & Rueda, F. J. (2014). Pathways of river water to the surface layers of stratified reservoirs. *Limnology and Oceanography*, 59(1), 233–250. <https://doi.org/10.4319/l.2014.59.1.0233>
- Deardorff, J. W. (1970). Convective velocity and temperature scales for the unstable planetary boundary layer and for Rayleigh convection. *Journal of the Atmospheric Sciences*, 27(8), 1211–1213. [https://doi.org/10.1175/1520-0469\(1970\)027<1211:cvatsf>2.0.co;2](https://doi.org/10.1175/1520-0469(1970)027<1211:cvatsf>2.0.co;2)
- Doda, T., Ramón, C. L., Ulloa, H. N., Wüest, A., & Bouffard, D. (2022). Seasonality of density currents induced by differential cooling. *Hydrology and Earth System Sciences*, 26(2), 331–353. <https://doi.org/10.5194/hess-26-331-2022>
- Driedonks, A. G. M. (1982). Models and observations of the growth of the atmospheric boundary layer. *Boundary-Layer Meteorology*, 23(3), 283–306. <https://doi.org/10.1007/BF00121117>
- Farrow, D. E. (2013). Periodically driven circulation near the shore of a lake. *Environmental Fluid Mechanics*, 13(3), 243–255. <https://doi.org/10.1007/s10652-012-9261-4>
- Farrow, D. E., & Patterson, J. C. (1993). On the response of a reservoir sidearm to diurnal heating and cooling. *Journal of Fluid Mechanics*, 246(1), 143–161. <https://doi.org/10.1017/S0022112093000072>
- Fer, I., Lemmin, U., & Thorpe, S. A. (2001). Cascading of water down the sloping sides of a deep lake in winter. *Geophysical Research Letters*, 28(10), 2093–2096. <https://doi.org/10.1029/2000GL012599>
- Fer, I., Lemmin, U., & Thorpe, S. A. (2002). Winter cascading of cold water in Lake Geneva. *Journal of Geophysical Research*, 107(C6), 3060. <https://doi.org/10.1029/2001JC000828>
- Fitchko, J., & Hutchinson, T. C. (1975). A comparative study of heavy metal concentrations in river mouth sediments around the Great Lakes. *Journal of Great Lakes Research*, 1(1), 46–78. [https://doi.org/10.1016/S0380-1330\(75\)72335-3](https://doi.org/10.1016/S0380-1330(75)72335-3)
- Haas, M., Baumann, F., Castella, D., Haghypour, N., Reusch, A., Strasser, M., et al. (2019). Roman-driven cultural eutrophication of Lake Murten, Switzerland. *Earth and Planetary Science Letters*, 505, 110–117. <https://doi.org/10.1016/j.epsl.2018.10.027>
- Harashima, A., & Watanabe, M. (1986). Laboratory experiments on the steady gravitational circulation excited by cooling of the water surface. *Journal of Geophysical Research*, 91(C11), 13056. <https://doi.org/10.1029/jc091ic11p13056>
- Hofmann, H. (2013). Spatiotemporal distribution patterns of dissolved methane in lakes: How accurate are the current estimations of the diffusive flux path? *Geophysical Research Letters*, 40(11), 2779–2784. <https://doi.org/10.1002/grl.50453>

- Hofmann, H., Federwisch, L., & Peeters, F. (2010). Wave-induced release of methane: Littoral zones as source of methane in lakes. *Limnology and Oceanography*, 55(5), 1990–2000. <https://doi.org/10.4319/lo.2010.55.5.1990>
- Hogg, C. A. R., Marti, C. L., Huppert, H. E., & Imberger, J. (2013). Mixing of an interflow into the ambient water of Lake Iseo. *Limnology and Oceanography*, 58(2), 579–592. <https://doi.org/10.4319/lo.2013.58.2.0579>
- Horwitz, R., & Lentz, S. J. (2014). Inner-shelf response to cross-shelf wind stress: The importance of the cross-shelf density gradient in an idealized numerical model and field observations. *Journal of Physical Oceanography*, 44(1), 86–103. <https://doi.org/10.1175/JPO-D-13-075.1>
- Jabbari, A., Ackerman, J. D., Boegman, L., & Zhao, Y. (2019). Episodic hypoxia in the western basin of Lake Erie. *Limnology and Oceanography*, 64(5), 2220–2236. <https://doi.org/10.1002/lno.11180>
- James, W. F., & Barko, J. W. (1991). Estimation of phosphorus exchange between littoral and pelagic zones during nighttime convective circulation. *Limnology and Oceanography*, 36(1), 179–187. <https://doi.org/10.4319/lo.1991.36.1.0179>
- James, W. F., Barko, J. W., & Eakin, H. L. (1994). Convective water exchanges during differential cooling and heating: Implications for dissolved constituent transport. *Hydrobiologia*, 294(2), 167–176. <https://doi.org/10.1007/BF00016857>
- Kandie, F. J., Krauss, M., Beckers, L. M., Massei, R., Fillinger, U., Becker, J., et al. (2020). Occurrence and risk assessment of organic micropollutants in freshwater systems within the Lake Victoria South Basin, Kenya. *Science of the Total Environment*, 714, 136748. <https://doi.org/10.1016/j.scitotenv.2020.136748>
- Lemmin, U. (2020). Insights into the dynamics of the deep hypolimnion of Lake Geneva as revealed by long-term temperature, oxygen, and current measurements. *Limnology and Oceanography*. <https://doi.org/10.1002/lno.11441>
- Lentz, S. J., & Fewings, M. R. (2012). The wind- and wave-driven inner-shelf circulation. *Annual Review of Marine Science*, 4, 317–343. <https://doi.org/10.1146/annurev-marine-120709-142745>
- Li, J., Liu, H., & Paul Chen, J. (2018). Microplastics in freshwater systems: A review on occurrence, environmental effects, and methods for microplastics detection. *Water Research*, 137, 362–374. <https://doi.org/10.1016/j.watres.2017.12.056>
- Lin, Y.-T. (2015). Wind effect on diurnal thermally driven flow in vegetated nearshore of a lake. *Environmental Fluid Mechanics*, 15(1), 161–178. <https://doi.org/10.1007/s10652-014-9368-x>
- MacIntyre, S., & Melack, J. M. (2009). Mixing dynamics in lakes across climatic zones. In *Encyclopedia of inland waters* (pp. 603–612). Elsevier Inc. <https://doi.org/10.1016/B978-012370626-3.00040-5>
- Mahjabin, T., Pattiaratchi, C., & Hetzel, Y. (2019). Wind effects on dense shelf water cascades in south-west Australia. *Continental Shelf Research*, 189, 103975. <https://doi.org/10.1016/j.csr.2019.103975>
- Mahjabin, T., Pattiaratchi, C., & Hetzel, Y. (2020). Occurrence and seasonal variability of dense shelf water cascades along Australian continental shelves. *Scientific Reports*, 10(1), 1–13. <https://doi.org/10.1038/s41598-020-66711-5>
- Mao, Y., Lei, C., & Patterson, J. C. (2019). Natural convection in a reservoir induced by sinusoidally varying temperature at the water surface. *International Journal of Heat and Mass Transfer*, 134, 610–627. <https://doi.org/10.1016/j.ijheatmasstransfer.2019.01.071>
- Marshall, J., Adcroft, A., Hill, C., Perelman, L., & Heisey, C. (1997). A finite-volume, incompressible Navier Stokes model for studies of the ocean on parallel computers. *Journal of Geophysical Research: Oceans*, 102(C3), 5753–5766. <https://doi.org/10.1029/96JC02775>
- Marshall, J., Hill, C., Perelman, L., & Adcroft, A. (1997). Hydrostatic, quasi-hydrostatic, and nonhydrostatic ocean modeling. *Journal of Geophysical Research: Oceans*, 102(C3), 5733–5752. <https://doi.org/10.1029/96JC02776>
- Marti, C. L., & Imberger, J. (2008). Exchange between littoral and pelagic waters in a stratified lake due to wind-induced motions: Lake Kinneret, Israel. *Hydrobiologia*, 603(1), 25–51. <https://doi.org/10.1007/s10750-007-9243-6>
- McDougall, T. J., Jackett, D. R., Wright, D. G., & Feistel, R. (2003). Accurate and computationally efficient algorithms for potential temperature and density of seawater. *Journal of Atmospheric and Oceanic Technology*, 20(5), 730–741. [https://doi.org/10.1175/1520-0426\(2003\)20<730:AAACEAF>2.0.CO;2](https://doi.org/10.1175/1520-0426(2003)20<730:AAACEAF>2.0.CO;2)
- Molina, L., Pawlak, G., Wells, J. R., Monismith, S. G., & Merrifield, M. A. (2014). Diurnal cross-shore thermal exchange on a tropical fore reef. *Journal of Geophysical Research: Oceans*, 119(9), 6101–6120. <https://doi.org/10.1002/2013JC009621>
- Monismith, S. G., Genin, A., Reidenbach, M. A., Yahel, G., Koseff, J. R., Monismith, S. G., et al. (2006). Thermally driven exchanges between a coral reef and the adjoining ocean. *Journal of Physical Oceanography*, 36(7), 1332–1347. <https://doi.org/10.1175/JPO2916.1>
- Monismith, S. G., Imberger, J., & Morison, M. L. (1990). Convective motions in the sidearm of a small reservoir. *Limnology and Oceanography*, 35(8), 1676–1702. <https://doi.org/10.4319/lo.1990.35.8.1676>
- Peeters, F., Finger, D., Hofer, M., Brennwald, M., Livingstone, D. M., & Kipfer, R. (2003). Deep-water renewal in Lake Issyk-Kul driven by differential cooling. *Limnology and Oceanography*, 48(4), 1419–1431. <https://doi.org/10.4319/lo.2003.48.4.1419>
- Perazzolo, C., Morasch, B., Kohn, T., Magnet, A., Thonney, D., & Chèvre, N. (2010). Occurrence and fate of micropollutants in the Vidy Bay of Lake Geneva, Switzerland. Part I: Priority list for environmental risk assessment of pharmaceuticals. *Environmental Toxicology and Chemistry*, 29(8). <https://doi.org/10.1002/etc.221>
- Phillips, O. M. (1966). On turbulent convection currents and the circulation of the Red Sea. *Deep-Sea Research and Oceanographic Abstracts*, 13(6), 1149–1160. [https://doi.org/10.1016/0011-7471\(66\)90706-6](https://doi.org/10.1016/0011-7471(66)90706-6)
- Ramón, C. L., Ulloa, H. N., Doda, T., Winters, K. B., & Bouffard, D. (2021). Bathymetry and latitude modify lake warming under ice. *Hydrology and Earth System Sciences*, 25(4), 1813–1825. <https://doi.org/10.5194/hess-25-1813-2021>
- Rao, Y. R., & Schwab, D. J. (2007). Transport and mixing between the coastal and offshore waters in the Great Lakes: A review. *Journal of Great Lakes Research*, 33(1), 202–218. [https://doi.org/10.3394/0380-1330\(2007\)33\[202:TAMBTC\]2.0.CO;2](https://doi.org/10.3394/0380-1330(2007)33[202:TAMBTC]2.0.CO;2)
- Read, J. S., Hamilton, D. P., Desai, A. R., Rose, K. C., MacIntyre, S., Lenters, J. D., et al. (2012). Lake-size dependency of wind shear and convection as controls on gas exchange. *Geophysical Research Letters*, 39(9). <https://doi.org/10.1029/2012GL051886>
- Roget, E., Colomer, J., Casamitjana, X., & Llebot, J. E. (1993). Bottom currents induced by baroclinic forcing in Lake Banyoles (Spain). *Aquatic Sciences*, 55(3), 206–227. <https://doi.org/10.1007/BF00877450>
- Rueda, F. J., Moreno-Ostos, E., & Cruz-Pizarro, L. (2007). Spatial and temporal scales of transport during the cooling phase of the ice-free period in a small high-mountain lake. *Aquatic Sciences*, 69(1), 115–128. <https://doi.org/10.1007/s00027-006-0823-8>
- Santiago-Mandujano, F., & Firing, E. (1990). Mixed-layer shear generated by wind stress in the central equatorial Pacific. *Journal of Physical Oceanography*, 20, 1576–1582. [https://doi.org/10.1175/1520-0485\(1990\)020<1576:mllsgbw>2.0.co;2](https://doi.org/10.1175/1520-0485(1990)020<1576:mllsgbw>2.0.co;2)
- Shapiro, G. I., Huthnance, J. M., & Ivanov, V. V. (2003). Dense water cascading off the continental shelf. *Journal of Geophysical Research*, 108(C12), 3390. <https://doi.org/10.1029/2002JC001610>
- Shintani, T., de la Fuente, A., de la Fuente, A., Niño, Y., & Imberger, J. (2010). Generalizations of the Wedderburn number: Parameterizing upwelling in stratified lakes. *Limnology and Oceanography*, 55(3), 1377–1389. <https://doi.org/10.4319/lo.2010.55.3.1377>
- Sighicelli, M., Pietrelli, L., Lecce, F., Iannilli, V., Falconieri, M., Coscia, L., et al. (2018). Microplastic pollution in the surface waters of Italian Subalpine Lakes. *Environmental Pollution*, 236, 645–651. <https://doi.org/10.1016/j.envpol.2018.02.008>

- Spigel, R. H., & Imberger, J. (1980). The classification of mixed-layer dynamics of lakes of small to medium size. *Journal of Physical Oceanography*, *10*(7), 1104–1121. [https://doi.org/10.1175/1520-0485\(1980\)010<1104:tcomld>2.0.co;2.CO;2](https://doi.org/10.1175/1520-0485(1980)010<1104:tcomld>2.0.co;2.CO;2)
- Sturman, J. J., & Ivey, G. N. (1998). Unsteady convective exchange flows in cavities. *Journal of Fluid Mechanics*, *368*(1), 127–153. <https://doi.org/10.1017/S002211209800175X>
- Sturman, J. J., Oldham, C. E., & Ivey, G. N. (1999). Steady convective exchange flows down slopes. *Aquatic Sciences*, *61*(3), 260. <https://doi.org/10.1007/s000270050065>
- Thevenon, F., Graham, N. D., Chiaradia, M., Arpagaus, P., Wildi, W., & Poté, J. (2011). Local to regional scale industrial heavy metal pollution recorded in sediments of large freshwater lakes in central Europe (lakes Geneva and Lucerne) over the last centuries. *Science of the Total Environment*, *412–413*, 239–247. <https://doi.org/10.1016/j.scitotenv.2011.09.025>
- Ulloa, H. N., Davis, K. A., Monismith, S. G., & Pawlak, G. (2018). Temporal variability in thermally driven cross-shore exchange: The role of semidiurnal tides. *Journal of Physical Oceanography*, *48*(7), 1513–1531. <https://doi.org/10.1175/JPO-D-17-0257.1>
- Ulloa, H. N., Ramón, C. L., Doda, T., Wüest, A., & Bouffard, D. (2022). Development of overturning circulation in sloping waterbodies due to surface cooling. *Journal of Fluid Mechanics*, *930*, A18. <https://doi.org/10.1017/jfm.2021.883>
- Ulloa, H. N., Winters, K. B., Wüest, A., & Bouffard, D. (2019). Differential heating drives downslope flows that accelerate mixed-layer warming in ice-covered waters. *Geophysical Research Letters*, *46*(23), 13872–13882. <https://doi.org/10.1029/2019GL085258>
- Verburg, P., Antenucci, J. P., & Hecky, R. E. (2011). Differential cooling drives large-scale convective circulation in Lake Tanganyika. *Limnology and Oceanography*, *56*(3), 910–926. <https://doi.org/10.4319/lo.2011.56.3.0910>
- Winters, K. B., Lombard, P. N., Riley, J. J., & D'Asaro, E. A. (1995). Available potential energy and mixing in density-stratified fluids. *Journal of Fluid Mechanics*, *289*, 115–128. <https://doi.org/10.1017/S002211209500125X>
- Woodward, B. L., Marti, C. L., Imberger, J., Hipsey, M. R., & Oldham, C. E. (2017). Wind and buoyancy driven horizontal exchange in shallow embayments of a tropical reservoir: Lake Argyle, Western Australia. *Limnology and Oceanography*, *62*(4), 1636–1657. <https://doi.org/10.1002/lno.10522>
- Wu, X., Cahl, D., & Voulgaris, G. (2018). Effects of wind stress and surface cooling on cross-shore exchange. *Journal of Physical Oceanography*, *48*(11), 2627–2647. <https://doi.org/10.1175/JPO-D-17-0216.1>
- Wüest, A., & Lorke, A. (2003). Small-scale hydrodynamics in lakes. *Annual Review of Fluid Mechanics*, *35*(1), 373–412. <https://doi.org/10.1146/annurev.fluid.35.101101.161220>
- Yakimovich, K. M., Orland, C., Emilson, E. J. S., Tanentzap, A. J., Basiliko, N., & Myktyczuk, N. C. S. (2020). Lake characteristics influence how methanogens in littoral sediments respond to terrestrial litter inputs. *The ISME Journal*, *14*(8), 2153–2163. <https://doi.org/10.1038/s41396-020-0680-9>
- Zilitinkevich, S. S. (1991). Turbulent penetrative convection. In B. Henderson-Sellers (Ed.), *Avebury Technical*.

Reference From the Supporting Information

- Jackett, D. R., & McDougall, T. J. (1995). Minimal adjustment of hydrographic profiles to achieve static stability. *Journal of Atmospheric and Oceanic Technology*, *12*(2), 381–389. [https://doi.org/10.1175/1520-0426\(1995\)012<0381:maohpt>2.0.co;2](https://doi.org/10.1175/1520-0426(1995)012<0381:maohpt>2.0.co;2)